ATLAS PUB Note
ATL-PHYS-PUB-2024-001
11th January 2024

Prospects for a search for direct pair production of top squarks at the high-luminosity LHC with the ATLAS detector

The ATLAS Collaboration

Prospects for a future search for direct pair production of top squarks (stop) in events with two opposite-charge leptons (electrons or muons), jets and missing transverse momentum at the HL-LHC are investigated in this note. The region of small mass-splitting between the stop and the lightest neutralino $\Delta m(\tilde{t}_1, \tilde{\chi}_1^0)$, where the stop proceeds through a four-body or three-body decay, without the presence of an on-shell top quark, is studied, and finally the analysis is also applied to the two-body decay region, where $\Delta m(\tilde{t}_1, \tilde{\chi}_1^0) > m(t)$. The analysis builds on a similar search, in this final state, published using 139 fb^{-1} of integrated luminosity from proton–proton collisions at $\sqrt{s} = 13$ TeV collected by the ATLAS detector during Run 2. The potential discovery reach and the 95% CL exclusion limits for $\sqrt{s} = 14$ TeV and an integrated luminosity of 3000 fb^{-1} are presented. In the four-body decay region the discovery sensitivity with a 5σ significance extends up to $m(\tilde{t}_1)$ of about 380 GeV for $\Delta m(\tilde{t}_1, \tilde{\chi}_1^0)$ of about 65 GeV and reaches about 480 GeV for $\Delta m(\tilde{t}_1, \tilde{\chi}_1^0)$ of about 25 GeV. The discovery potential at 5σ extends up to stop masses of about 660 GeV for a $\tilde{\chi}_1^0$ mass of about 490 GeV in the three-body decay region and up to about 810 GeV for a massless $\tilde{\chi}_1^0$ in the two-body decay region. The 95% CL exclusion limit extends up to $m(\tilde{t}_1)$ of about 690 GeV, for a $\tilde{\chi}_1^0$ mass of about 660 GeV in the four-body decay region, up to $m(\tilde{t}_1)$ of about 850 GeV for a $\tilde{\chi}_1^0$ mass of about 680 GeV in the three-body decay region and up to $m(\tilde{t}_1)$ of about 1010 GeV for a massless $\tilde{\chi}_1^0$ in the two-body decay region, covering a significant region beyond the current limits.

1 Introduction

The upgraded HL-LHC is planned to deliver proton-proton collisions at a center-of-mass energy of $\sqrt{s}$ = 14 TeV with a nominal instantaneous luminosity of 5 $\times 10^{34}$ cm^{-2}s^{-1} and a maximum instantaneous luminosity of 7.5 $\times 10^{34}$ cm^{-2}s^{-1}. In these conditions, the average number of collisions per bunch crossing, or pile-up μ, will increase up to approximately 200. The HL-LHC phase will allow the ATLAS and CMS experiments to each collect an integrated luminosity of about 3000 fb^{-1}.

This note estimates the sensitivity of future ATLAS searches for direct pair production of top squarks at the HL-LHC. In the models targeted by this search R-parity is assumed to be conserved. This implies that SUSY particles are produced in pairs and the lightest supersymmetric particle (LSP) is stable and weakly interacting [1].

A previous note [2] investigated the sensitivity in the region of large $\Delta m(\tilde{t}_1, \tilde{\chi}_1^0) = m(\tilde{t}_1) - m(\tilde{\chi}_1^0)$, where the stop decay proceeds through the two-body channel into an on-shell top quark and the lightest neutralino ($\tilde{t}_1 \rightarrow t\tilde{\chi}_1^0$). Fully hadronic decay modes of the top quark were considered selecting events with jets and b-jets.

In this note the region where $\Delta m(\tilde{t}_1, \tilde{\chi}_1^0) < m(t)$, is studied. In this regime the decay of the stop proceeds through a three-body decay or a four-body decay, without the presence of an on-shell top quark. Finally the analysis is also applied to the two-body decay region, where $\Delta m(\tilde{t}_1, \tilde{\chi}_1^0) > m(t)$. In the three-body decay mode, for which $\Delta m(\tilde{t}_1, \tilde{\chi}_1^0) - m(b) > m(W)$, the stop decays into an on-shell W boson, a b-quark and the lightest neutralino ($\tilde{t}_1 \rightarrow bW\tilde{\chi}_1^0$) and in the four-body decay mode, for which $\Delta m(\tilde{t}_1, \tilde{\chi}_1^0) - m(b) < m(W)$, into a b-quark, two fermions and the lightest neutralino ($\tilde{t}_1 \rightarrow bff'\tilde{\chi}_1^0$). The two fermions f and f' are, in this note, a lepton (anti-lepton) with its anti-neutrino (neutrino). Events with two opposite-charge leptons (electrons or muons), jets and missing transverse momentum are considered. Since the analysis shows good sensitivity, for completeness, the results are also extended to the two-body decay region. The decay modes targeted by the search are shown in Figure 1.

The overall strategy was already applied [3] using the full luminosity collected by the ATLAS detector at $\sqrt{s}$ = 13 TeV during Run 2 (2015–2018). The same strategy and final object reconstruction criteria are used in this note. However, the event selection is further optimised to maximise the sensitivity across a wide range of $\Delta m(\tilde{t}_1, \tilde{\chi}_1^0)$, under the assumption of an integrated luminosity of 3000 fb^{-1}. To this purpose, the requirement on each variable used for the event selection is chosen by looking at the distribution of the variable for the SM background and for two benchmark signal models after all other selection requirements are applied, except the one on the variable itself.

2 ATLAS detector

The ATLAS detector at the LHC covers nearly the entire solid angle around the collision point and is described elsewhere [4]. The detector will undergo an extensive upgrade for the HL-LHC phase (Phase-2 upgrade) to allow efficient data taking and event reconstruction in conditions of higher luminosity with an expected pile-up of additional interactions per bunch crossing reaching μ=200. A detailed overview of the detector upgrades is given in Refs [5–12]. The upgrades of the detector aim at maintaining the current level of performance in physics object reconstruction or even improving them. The current Inner Detector (ID) will be substituted by a new Inner Tracker (ITk), which will cover the region up to $|\eta| < 2.7$ with

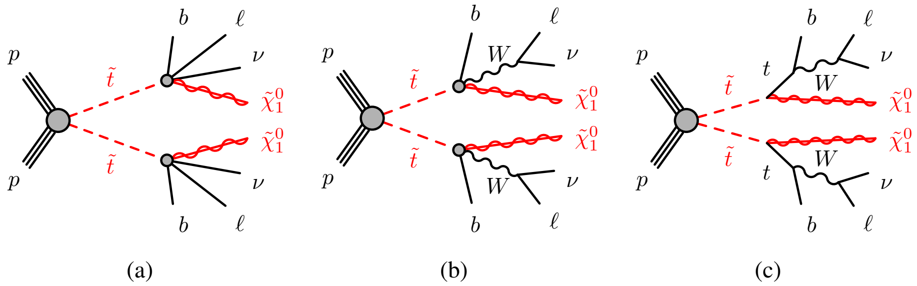

Figure 1: Diagrams representing the signal models targeted by the search presented in this note: (a) the four-body $\tilde{t}_1$ decay mode ($\tilde{t}_1 \rightarrow b\ell\nu\tilde{\chi}_1^0$) where ℓ and ν are a lepton (anti-lepton) with its anti-neutrino (neutrino), (b) the three-body $\tilde{t}_1$ decay mode into an on-shell W boson, a b-quark and the lightest neutralino ($\tilde{t}_1 \rightarrow bW\tilde{\chi}_1^0$), and (c) the two-body $\tilde{t}_1$ decay into an on-shell top quark and the lightest neutralino ($\tilde{t}_1 \rightarrow t\tilde{\chi}_1^0$). For all the diagrams (a-c) the distinction between particle and anti-particle is omitted.

a strip detector and up to $|\eta| < 4$ with a pixel detector. This will significantly increase the coverage of precise tracking. As an example, the jet b-tagging algorithms will fully use the pixel detector coverage, which is currently limited to $|\eta| < 2.5$. When restricted to the range of the current detector ($|\eta| < 2.5$) the tracking performances of ITk, the performance of vertex reconstruction, pile-up jet rejection and jet flavour tagging, illustrated in Ref. [13], are expected to maintain or even exceed the Run 2 performance level. The trigger system will also be replaced in order to maintain or lower the current thresholds, so that equal or improved performance can be expected.

For these projection studies at HL-LHC the background contribution estimates are based on a full detector simulation (GEANT4 [14], and normalised to the cross-sections expected at the HL-LHC collision energy and for an integrated luminosity of 3000 fb^{-1}. The data driven corrections to these estimates are based on the results of the Run 2 analysis [3]. The signal predictions are based on a simulation performed considering the layout and the response of the ATLAS detector, using the Run 2 layout and by applying a set of smearing functions at generator level to final-state particles. The smearing functions have been determined from a full GEANT4 simulation of the ATLAS detector. The signal yields are normalised to the cross-sections expected at the HL-LHC collision energy and for an integrated luminosity of 3000 fb^{-1}. Background and signal predictions do not account for improvements coming from the upgraded ATLAS detector. Object reconstruction and identification efficiencies at the HL-LHC are assumed to be identical to that used for the analysis of Run 2 [3]. Moreover, in the upgraded detector for the HL-LHC, we expect to be able to lower the trigger thresholds for many of these objects, and this analysis could benefit from this [15]. The resolutions on the variables relevant for the analysis, like $E_{\mathrm{T}}^{\mathrm{miss}}$, could change in the upgraded detector, but we are assuming here the same performance as in Run 2, as well. Due to all these considerations, the sensitivity estimates obtained can be considered conservative.

3 Event simulation

The analysis uses datasets of Standard Model (SM) background and supersymmetric signal processes simulated using different event generators as detailed below. All samples are generated at 13 TeV and scaled to the 14 TeV cross-sections. Changes in kinematics from the higher centre of mass energy are not accounted for, but very preliminary studies performed on some benchmark signals showed that these changes introduced a marginal increase in signal significance Z_n [16].

The SM background contributions are evaluated using Monte Carlo (MC) simulation samples. All SM processes accounted for are summarised in Table 1.These samples are processed through a full GEANT4 [14] simulation of the ATLAS detector. The dominant background processes are VV and VVV production, $t\bar{t}$ and single top. Cross-sections are extrapolated to the energy of 14 TeV by scaling with the appropriate factors for each sample, specifically 10% for VV, 20% for $t\bar{t}+Z$, 9% for V+jets and 18% for $t\bar{t}$, Wt and all other backgrounds [17, 18].

Stop pair production events are generated with matrix element (ME) calculations at tree level (LO) and with up to two additional partons using aMC@NLO 2.6.2 [19]. The ME generation is interfaced to PYTHIA 8.212 and MADSPIN [20, 21] for the parton showering (PS), hadronisation, and for the b and c hadron decays. The parton distribution function (PDF) used for the generation of the signal samples is the NNPDF2.3LO set [22] with the A14 [23] tune of underlying-event and shower parameters. The ME-PS matching is performed with the CKKW-L prescription [24], with a matching scale set to one quarter of the mass of the stop. The signal samples are processed using a set of smearing functions (applied at generator level) to emulate the ATLAS detector [13, 25].

All signal cross-sections are calculated at next-to-next-to-leading order (NNLO) in α_s, adding the resummation of soft gluon emission at next-to-next-to-leading-logarithm accuracy (NNLO+NNLL) [26–33]. They strongly depend on the stop mass: for example, the stop pair production cross-section is 610 (6.8) fb for a stop mass of 500 (1000) GeV. The signal cross-sections are extrapolated to 14 TeV using the ratio of NNLO calculations which are available at both energies. For example the scale factor is 1.28 (1.40) for a stop mass of 500 (1000) GeV.

Table 1: Summary of the generators used for signal and background processes. The matrix element (ME) and parton shower (PS) generators, the cross-section order in α_s used to normalise the event yield, and the PDF sets used in ME and PS are reported.

Physics process	Generator	Parton shower	Normalisation	PDF (generator)	PDF (PS)
SUSY Signals	MADGRAPH5_aMC@NLO [19].	PYTHIA 8.212 [34, 35]	NNLO+NNLL [26–33]	NNPDF2.3LO [22]	NNPDF2.3LO
$t\bar{t}$	POWHEG-BOX v2 [36–38]	PYTHIA 8.230	NNLO+NNLL [39]	NNPDF3.0NLO [40]	NNPDF2.3LO
$t\bar{t}+V$ $(V=W,Z)$	MADGRAPH5_aMC@NLO	PYTHIA 8.210	NLO [19, 41]	NNPDF3.0NLO	NNPDF2.3LO
Single top	POWHEG-BOX v2 [36–38, 42, 43]	PYTHIA 8.230	NLO+NNLL [44–47]	NNPDF3.0NLO	NNPDF2.3LO
$Z/\gamma^*(\rightarrow \ell\ell)$+jets	SHERPA 2.2.1 [48, 49]	SHERPA 2.2.1	NNLO [50]	NNPDF3.0NNLO [40]	NNPDF3.0NNLO
Diboson VV $(V=W,Z)$	SHERPA 2.2.1 or 2.2.2 [48]	SHERPA 2.2.1 or 2.2.2	NLO [51]	NNPDF3.0NNLO	NNPDF3.0NNLO
Triboson VVV $(V=W,Z)$	SHERPA 2.2.2	SHERPA 2.2.2	NLO [48, 51]	NNPDF3.0NNLO	NNPDF3.0NNLO
$t\bar{t}H$	POWHEG-BOX v2 [36, 37, 52]	PYTHIA 8.230	NLO [19, 41]	NNPDF3.0NLO	NNPDF2.3LO
$t\bar{t}WW$	MADGRAPH5_aMC@NLO	PYTHIA 8.186 [34]	NLO [19]	NNPDF2.3LO	NNPDF2.3LO
$t\bar{t}WZ$	MADGRAPH5_aMC@NLO	PYTHIA 8.212	NLO [19]	NNPDF3.0NLO	NNPDF2.3LO
$tZ, t\bar{t}t\bar{t}, t\bar{t}t$	MADGRAPH5_aMC@NLO	PYTHIA 8.230	NLO [19]	NNPDF3.0NLO	NNPDF2.3LO

4 Object definitions

The criteria used for the objected definition are similar to those applied in Ref. [3]. A short description is provided here. Leptons are classified as baseline or signal depending on an increasingly stringent set of reconstruction quality criteria and kinematic selections. Signal leptons are a subset of the baseline leptons. Baseline leptons are used in the calculation of the missing transverse momentum ($\mathbf{p}_{\mathrm{T}}^{\mathrm{miss}}$, with magnitude

$E_{\mathrm{T}}^{\mathrm{miss}}$), and to resolve ambiguities between analysis objects in the event, while signal leptons are used for the final event selection.

Electrons are reconstructed by matching ID tracks with three-dimensional clusters of energy deposits in the electromagnetic calorimeter. Signal electrons are required to have $E_{\mathrm{T}} > 4.5\,\mathrm{GeV}$ and $|\eta| < 2.47$, and to pass a *Medium* likelihood-based identification requirement [53] with additional conditions on the track and on the transverse impact parameter. Isolation criteria are applied to electrons by placing an upper bound on the sum of the transverse energy of the calorimeter energy clusters, and on the the scalar sum of the p_{T} of tracks within certain cones around the electron direction.

Muons are reconstructed by matching ID tracks with Muon Spectrometer (MS) tracks or energy deposits in the calorimeter compatible with a minimum-ionising particle. The resulting tracks are required to have $p_{\mathrm{T}} > 4\,\mathrm{GeV}$ and $|\eta| < 2.7$, for the four-body selections, and $|\eta| < 2.4$ for the three-body selection, and to satisfy the *Medium* identification requirement [54] based on the numbers of hits in the different ID and MS subsystems; on the significances of the charge-to-momentum ratio q/p, and on the transverse impact parameter from the primary vertex. Isolation criteria similar to that for electrons are also applied.

In the four-body region the background coming from fake and non-prompt leptons (FNP), originating from π/K and heavy- flavour hadron decays and photon conversions, is important, due to the low-p_{T} requirements in the lepton selection. This background is estimated from data using the 'fake factor' method [55–58], as described in Ref. [3]. The 'fake factor' method uses two orthogonal lepton definitions, labelled as 'Id' (passing signal lepton identification criteria) and 'anti-Id' (failing either the signal identification or isolation requirement for electrons and the isolation requirement for muons), to define a control data sample enriched in fake leptons. The fake factor is defined as the ratio of the Id lepton yield to the anti-Id probe lepton yield and it is measured separately for electrons and muons and as a function of the lepton p_T and η. The FNP estimates in each analysis region are derived by applying the fake factors to events satisfying that region's criteria but replacing at least one of the signal leptons by an anti-Id one. At HL-LHC the FNP background rejection could benefit from the higher granularity of the upgraded detector and from the improved performance of the isolation algorithms.

Jets are reconstructed from three-dimensional clusters of energy in the calorimeter using the anti-k_t jet clustering algorithm with a radius parameter $R = 0.4$ and required to have $p_{\mathrm{T}} > 20\,\mathrm{GeV}$ and $|\eta| < 2.8$. To reduce the effects of pile-up, for jets with $p_{\mathrm{T}} < 60\,\mathrm{GeV}$ a significant fraction of the tracks associated with each jet are required to have an origin compatible with the primary vertex, as defined by the jet vertex tagger [59] (JVT). This requirement reduces the fraction of jets from pile-up to 1%, with an efficiency for pure hard-scatter jets of about 90%. Jets containing b-hadrons ('b-jets') are identified in the range $|\eta| < 2.5$, using a boosted decision tree algorithm (MV2c10 [60]) which uses quantities such as the impact parameters of associated tracks, and well-reconstructed secondary vertices. A working point which provides 77% efficiency for tagging b-jets in simulated $t\bar{t}$ events is used. Corresponding rejection factors against jets originating from c-quarks, from τ-leptons, and from light quarks and gluons are 4.9, 15 and 110, respectively.

The missing transverse momentum is defined as the negative vector sum of the transverse momenta for all baseline electrons, muons and jets, and of an additional "soft term" including all low-momentum tracks that pass basic quality requirements and are associated with the primary vertex but not with any reconstructed physics object [61]. Linked to the $E_{\mathrm{T}}^{\mathrm{miss}}$ value is the 'object-based $E_{\mathrm{T}}^{\mathrm{miss}}$ significance' [62], which measures the $E_{\mathrm{T}}^{\mathrm{miss}}$ significance based upon the transverse momentum resolution of all objects used in the calculation of the $\mathbf{p}_{\mathrm{T}}^{\mathrm{miss}}$. The $E_{\mathrm{T}}^{\mathrm{miss}}$ significance helps to separate events with true $E_{\mathrm{T}}^{\mathrm{miss}}$ originating from weakly interacting particles such as neutrinos or neutralinos, from events where $E_{\mathrm{T}}^{\mathrm{miss}}$ is consistent with particle mis-measurement, resolution or identification inefficiencies.

5 Event selections

Two different event selections, as described below, target the four-body and three-body decay modes. Events are required to have exactly two signal leptons (two electrons, two muons, or one electron and one muon) with opposite electric charge. The four-body selection uses a soft p_{T} threshold of 5 GeV for the leptons, which improves the analysis sensitivity by removing the FNP background contribution, larger at lower p_{T} values. The three-body selection uses a 25 GeV and a 20 GeV p_{T} threshold, for the leading and sub-leading leptons, respectively. Both selections use the $E_{\mathrm{T}}^{\mathrm{miss}}$ significance variable. Different jet (b-jet) multiplicities, labelled as n_{jets} ($n_{b-\mathrm{jets}}$), are required in the two selections. Different kinematic variables are exploited to separate the signal from the SM background, described below. A complete description and derivation of the variables can be obtained in Ref. [3].

In Ref. [3], events in the four-body region were triggered by the $E_{\mathrm{T}}^{\mathrm{miss}}$ trigger, while in the three-body region they were selected by a di-lepton trigger. The same strategy is considered for these selections.

5.1 Four-body selection

The stop four-body decay, as shown in Figure 1(a), can proceed through an off-shell top quark and W boson decay in the kinematic region defined by $m(b) < \Delta m(\tilde{t}_1, \tilde{\chi}_1^0) < m(b) + m(W)$. The leptons from the virtual W boson decay are expected to have low transverse momentum and can be efficiently selected when imposing both lower and upper bounds on the p_{T} of the leptons. A transverse momentum lower bound of 5 GeV is applied to electrons and muons together with an upper bound, which is optimised separately for the leading and sub-leading leptons.

Two orthogonal signal regions are defined: the first one, $\mathrm{SR}^{4-\mathrm{body}}_{\mathrm{Small}\,\Delta m}$, targets small values of $\Delta m(\tilde{t}_1, \tilde{\chi}_1^0)$ and requires $p_{\mathrm{T}}(\ell_1) \in [5, 25]$ GeV range and $p_{\mathrm{T}}(\ell_2) \in [5, 10]$ GeV range; the second one, $\mathrm{SR}^{4-\mathrm{body}}_{\mathrm{Large}\,\Delta m}$, targets larger values of $\Delta m(\tilde{t}_1, \tilde{\chi}_1^0)$ and instead requires $p_{\mathrm{T}}(\ell_1) \in [10, 100]$ GeV range and $p_{\mathrm{T}}(\ell_2) \in [10, 20]$ GeV range, where the upper bound on $p_{\mathrm{T}}(\ell_2)$ of 20 GeV is used to make this selection orthogonal to the three-body one.

In order to select events with a large enough $E_{\mathrm{T}}^{\mathrm{miss}}$ to be above the trigger threshold, we consider events in which an energetic initial-state radiation (ISR) jet recoils against the two top squarks, boosting the system and enhancing the total $E_{\mathrm{T}}^{\mathrm{miss}}$ originating from all neutrinos and neutralinos in the event above the $E_{\mathrm{T}}^{\mathrm{miss}}$ trigger threshold. The leading jet j_1 is assumed to be a jet from ISR and is required to have $p_{\mathrm{T}} > 150$ GeV. The leptons invariant mass $m_{\ell\ell}$ is required to be greater than 10 GeV to remove leptons from Drell–Yan and low-mass resonances. A further reduction of the SM background is achieved with selections on $E_{\mathrm{T}}^{\mathrm{miss}}$ significance, $p_{\mathrm{T,boost}}^{\ell\ell}$, $R_{2\ell}$ and $R_{2\ell 4j}$ variables [3]. A requirement is applied to improve the sub-leading lepton isolation, using the following isolation variable:

$$\min \Delta R_{\ell_2, j_i} = \min_{j_i \in [\mathrm{jets}]} \Delta R(\ell_2, j_i)$$

where ‘[jets]’ contains all the jets in the event. This reduces the probability of lepton misidentification or selecting a lepton originating from heavy-flavour or π/K decays in jets. The definitions of the signal regions are summarised in Table 2.

Table 2: Summary of the event selections for the two four-body signal regions. In order to improve the sensitivity of the four-body selection at the high-luminosity LHC, requirements on $E_{\mathrm{T}}^{\mathrm{miss}}$ significance, $p_{\mathrm{T,boost}}^{\ell\ell}$, $E_{\mathrm{T}}^{\mathrm{miss}}$ and $R_{2\ell 4j}$ are different from the ones applied in Ref. [3].

	$\mathrm{SR}^{4-\mathrm{body}}_{\mathrm{Small}\,\Delta m}$	$\mathrm{SR}^{4-\mathrm{body}}_{\mathrm{Large}\,\Delta m}$
$p_{\mathrm{T}}(\ell_1)$ [GeV]	$[5,\ 25]$	$[10,\ 100]$
$p_{\mathrm{T}}(\ell_2)$ [GeV]	$[5,\ 10]$	$[10,\ 20]$
$m_{\ell\ell}$ [GeV]	> 10	
$p_{\mathrm{T}}(j_1)$ [GeV]	> 150	
$\min \Delta R_{\ell_2, j_i}$	> 1	
$E_{\mathrm{T}}^{\mathrm{miss}}$ significance	> 10	> 18
$p_{\mathrm{T,boost}}^{\ell\ell}$ [GeV]	> 450	
$E_{\mathrm{T}}^{\mathrm{miss}}$ [GeV]	> 500	
$R_{2\ell}$	> 25	> 13
$R_{2\ell 4j}$	> 0.45	> 0.44

The distributions of these variables for both signal regions are shown in Figures 2 and 3. The distributions include all the backgrounds and two benchmark signal points for each region, specifically a $\Delta m = 20$ GeV point for $\mathrm{SR}^{4-\mathrm{body}}_{\mathrm{Small}\,\Delta m}$, $\Delta m = 80$ GeV point for $\mathrm{SR}^{4-\mathrm{body}}_{\mathrm{Large}\,\Delta m}$ and a $\Delta m = 50$ GeV for both. Black and red arrows indicate the selection thresholds as applied on these variables in Ref. [3] and in this note, respectively, thus pointing out the performed optimization.

Table 3 summarises the expected SM background contributions to the signal regions $\mathrm{SR}^{4-\mathrm{body}}_{\mathrm{Small}\,\Delta m}$ and $\mathrm{SR}^{4-\mathrm{body}}_{\mathrm{Large}\,\Delta m}$, where ‘Others’ includes contributions from single top, Z+jets, VVV, $t\bar{t}t$, $t\bar{t}t\bar{t}$, $t\bar{t}+V$, $t\bar{t}+VV$, $t\bar{t}H$, and tZ processes.

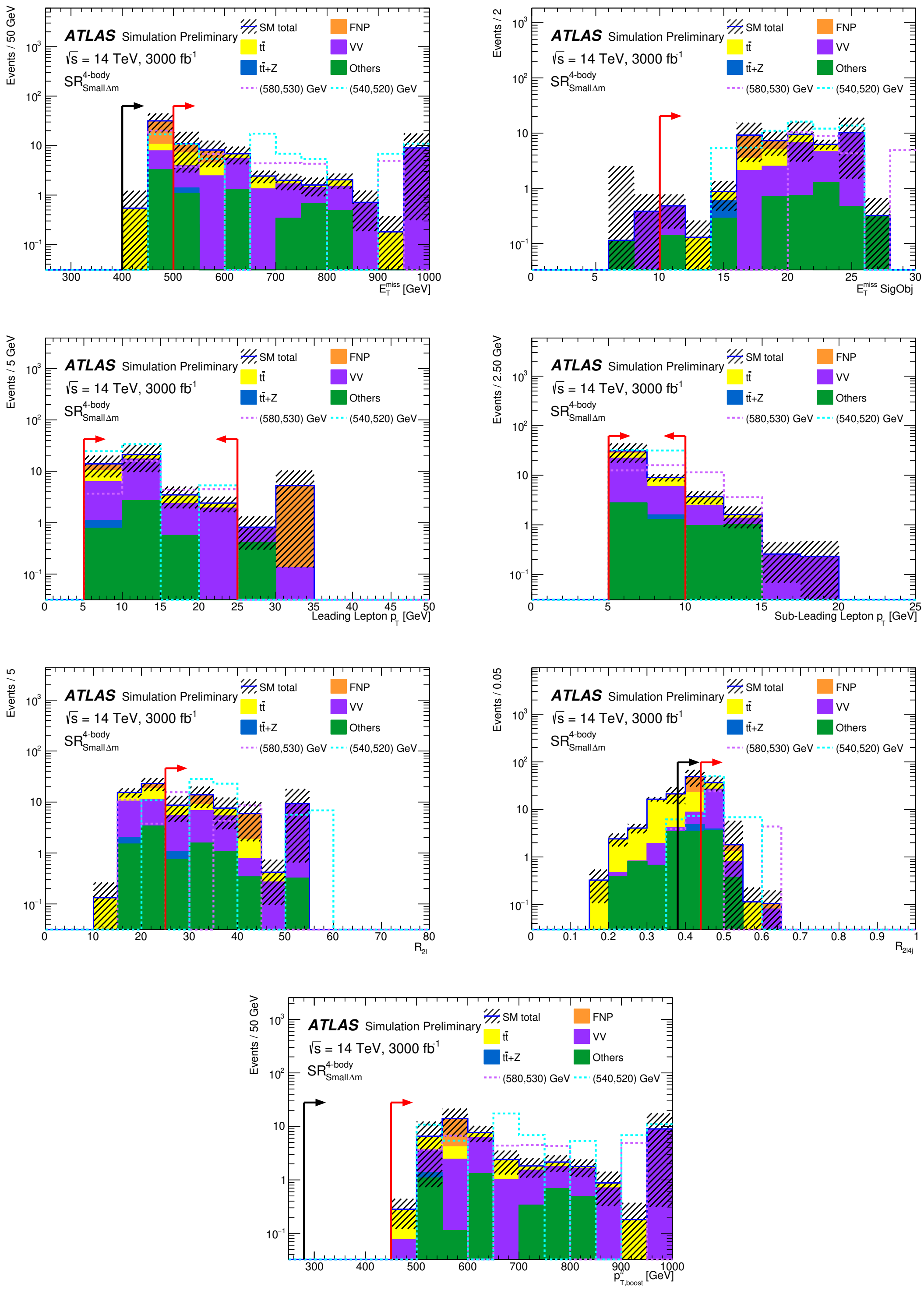

Figure 2: Distributions of the variables included in the optimised definition of SR$^{4-\text{body}}_{\text{Small}\,\Delta m}$ for the SM background and for two benchmark signal points. All selection requirements are applied to the events entering these distributions but the one on the plotted observable. Black and red arrows indicate the thresholds as used in Ref. [3] and in this note, respectively. The statistical uncertainty is shown on the total background as a shaded area. The final bin in each histogram includes the overflow.

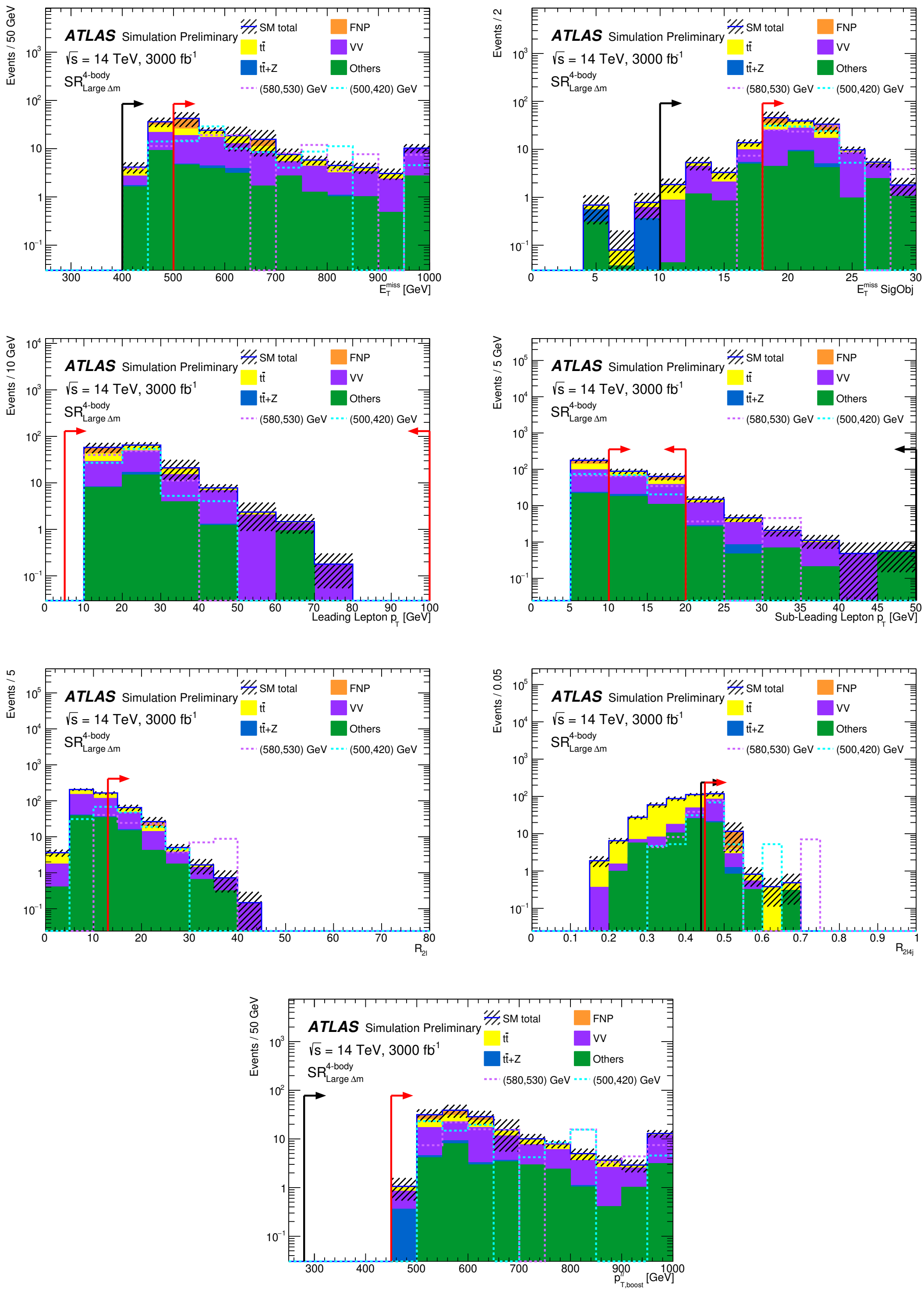

Figure 3: Distributions of the variables included in the optimised definition of $\mathrm{SR}^{4-\mathrm{body}}_{\mathrm{Large}\,\Delta m}$ for the SM background and for two benchmark signal points. All selection requirements are applied to the events entering these distributions but the one on the plotted observable. Black and red arrows indicate the thresholds as used in Ref. [3] and in this note, respectively. The statistical uncertainty is shown on the total background as a shaded area. The final bin in each histogram includes the overflow.

Table 3: Expected background and signal yields in $\mathrm{SR}^{4-\mathrm{body}}_{\mathrm{Small}\,\Delta m}$ and $\mathrm{SR}^{4-\mathrm{body}}_{\mathrm{Large}\,\Delta m}$ for an integrated luminosity of 3000 fb^{-1}. The uncertainties include both the statistical and systematic contributions.

Expected Background	$\mathrm{SR}^{4-\mathrm{body}}_{\mathrm{Small}\,\Delta m}$	$\mathrm{SR}^{4-\mathrm{body}}_{\mathrm{Large}\,\Delta m}$
Total SM events	40 ± 13	126 ± 25
MC VV events	23 ± 10	62 ± 18
MC $t\bar{t}$ events	8.0 ± 2.8	25 ± 5
MC $t\bar{t}$ +Z events	$0.24^{+0.51}_{-0.24}$	1.45 ± 0.29
MC Others events	3.9 ± 1.3	21 ± 5
FNP events	4.4 ± 1.4	16 ± 9
$m(\tilde{t}_1, \tilde{\chi}^0_1) = (540, 520)$ GeV events	63.7	–
$m(\tilde{t}_1, \tilde{\chi}^0_1) = (500, 420)$ GeV events	9.9	90.2
$m(\tilde{t}_1, \tilde{\chi}^0_1) = (580, 530)$ GeV events	28.5	92.0

5.2 Three-body selection

The three-body decay mode of the top squark shown in Figure 1(b) is dominant in the region where $m(W) + m(b) < \Delta m(\tilde{t}_1, \tilde{\chi}^0_1) < m(t)$.

The selection uses a set of kinematic quantities known as "Super-Razor" variables [3]. These are defined considering the different physics objects in a reference frame (the R frame) where the two leptons have equal and opposite p_z. For instance, $1/\gamma_{\mathrm{R}+1}$ is called "visible shape" and is a measure of how leptons are distributed, approaching zero when the leptons are back to back or have different momenta and approaching one when the leptons have similar momenta and are collinear. $R_{p_{\mathrm{T}}}$ is the vector sum of the transverse momenta of the visible particles and the missing transverse momentum. The azimuthal angle $\Delta\phi^{\mathrm{R}}_{\beta}$ is defined between the razor boost from the laboratory to the R frame and the sum of the visible momenta as evaluated in the R frame. It is a good discriminator when used in searches for signals from models with small mass differences between the massive pair-produced particle and the invisible particle produced in the decay. Finally, the variable is M^{R}_{Δ} is particularly powerful in discriminating between signal events and $t\bar{t}$ and diboson background, since it has a kinematic end-point that is proportional to the mass-splitting between the parent particle and the invisible particle.

The b-jet multiplicity is highly dependent on the mass-splitting between the top squark and the neutralino, since for lower $\Delta m(\tilde{t}_1, \tilde{\chi}^0_1)$ the b-jets have lower momentum and cannot be reconstructed efficiently. Two orthogonal signal regions (SRs) are defined: the $\mathrm{SR}^{3-\mathrm{body}}_{W}$ targeting $\Delta m(\tilde{t}, \tilde{\chi}^0_1) \sim m(W)$ with a b-jet veto, and the $\mathrm{SR}^{3-\mathrm{body}}_{t}$ targeting $\Delta m(\tilde{t}, \tilde{\chi}^0_1) \sim m(t)$ with at least one b-jet. Events with same-flavour (SF) or different-flavour (DF) lepton pairs are analysed separately, thus defining four different SRs: $\text{SR-DF}^{3-\mathrm{body}}_{W}$, $\text{SR-SF}^{3-\mathrm{body}}_{W}$, $\text{SR-DF}^{3-\mathrm{body}}_{t}$ and $\text{SR-SF}^{3-\mathrm{body}}_{t}$.

Events with same flavour lepton pairs ($e^{\pm}e^{\mp}$ and $\mu^{\pm}\mu^{\mp}$) with $m_{\ell\ell}$ between 71.2 and 111.2 GeV are rejected to reduce the Z boson background.

The signal regions make use of a common set of requirements on the p_{T} of the two leptons and $1/\gamma_{\mathrm{R}+1}$, and different requirements on the other variables like $E^{\mathrm{miss}}_{\mathrm{T}}$ significance, and "Super Razor variables" $\Delta\phi^{\mathrm{R}}_{\beta}$, $R_{p_{\mathrm{T}}}$, and M^{R}_{Δ}, as summarised in Table 4.

A di-lepton invariant mass $m_{\ell\ell}$ greater than 20 GeV is required to remove events from Drell–Yan and low-mass resonances.

Table 4: Summary of the event selections for the four three-body signal regions. In order to improve the sensitivity of the three-body selection at the high-luminosity LHC, requirements on $E_{\mathrm{T}}^{\mathrm{miss}}$ significance, $1/\gamma_{\mathrm{R+1}}$, $R_{p_{\mathrm{T}}}$ and M_{Δ}^{R} are different from the ones applied in Ref. [3].

	$\mathrm{SR}_{W}^{3-\mathrm{body}}$		$\mathrm{SR}_{t}^{3-\mathrm{body}}$	
Leptons flavour	DF	SF	DF	SF
$p_{\mathrm{T}}(\ell_1)$ [GeV]	> 25		> 25	
$p_{\mathrm{T}}(\ell_2)$ [GeV]	> 20		> 20	
$m_{\ell\ell}$ [GeV]	> 20		> 20	
$\lvert m_{\ell\ell} - m_Z \rvert$ [GeV]	–	> 20	–	> 20
$n_{b-\mathrm{jets}}$	$= 0$		≥ 1	
$\Delta\phi_{\beta}^{\mathrm{R}}$ [rad]	> 2.3		> 2.3	
$E_{\mathrm{T}}^{\mathrm{miss}}$ significance	> 15		> 14	
$1/\gamma_{\mathrm{R+1}}$	> 0.76		> 0.76	
$R_{p_{\mathrm{T}}}$	> 0.78		> 0.75	
M_{Δ}^{R} [GeV]	> 110		> 132	

Table 5.2 summarises the expected SM background contributions to the signal regions $\mathrm{SR}_{W}^{3-\mathrm{body}}$ and $\mathrm{SR}_{t}^{3-\mathrm{body}}$, where 'Others' includes contributions from single top, Z+jets, VVV, $t\bar{t}t$, $t\bar{t}t\bar{t}$, $t\bar{t}+V$, $t\bar{t}+VV$, $t\bar{t}H$, and tZ processes. The FNP background contribution is negligible.

Figures 4 and 5 show the distributions of the main observables used in the $\mathrm{SR}_{W}^{3-\mathrm{body}}$ and $\mathrm{SR}_{t}^{3-\mathrm{body}}$ selections, respectively. The distributions are shown for all backgrounds and for four benchmark signal points ranging between $\Delta m = 90$ GeV and $\Delta m = 165$ GeV. The new optimized selections are compared to those used in Ref. [3]. All selection requirements are applied to the events entering these distributions but the cut on the

Table 5: Expected background and signal yields for $\mathrm{SR}_{W}^{3-\mathrm{body}}$ and $\mathrm{SR}_{t}^{3-\mathrm{body}}$, separated in DF and SF events, for an integrated luminosity of 3000 fb^{-1}. The uncertainties include both the statistical and systematic contributions. The FNP background contribution is negligible.

Expected Background	$\mathrm{SR}_{W}^{3-\mathrm{body}}$ DF	$\mathrm{SR}_{W}^{3-\mathrm{body}}$ SF	$\mathrm{SR}_{t}^{3-\mathrm{body}}$ DF	$\mathrm{SR}_{t}^{3-\mathrm{body}}$ SF
Total SM events	29 ± 9	39 ± 13	35 ± 9	20 ± 9
MC VV events	19 ± 7	32 ± 12	2.3 ± 1.7	2.4 ± 1.1
MC $t\bar{t}$ events	5.0 ± 2.8	$1.4^{+4.9}_{-1.4}$	10 ± 4	2.4 ± 1.8
MC $t\bar{t}$ +Z events	$0.6^{+0.9}_{-0.6}$	1.4 ± 0.6	16 ± 4	11 ± 7
MC Others events	4.3 ± 1.2	4.2 ± 0.9	6.8 ± 1.4	3.5 ± 1.4
$m(\tilde{t}_1, \tilde{\chi}_1^0) = (550, 385)$ GeV events	24.9	–	91.4	58.6
$m(\tilde{t}_1, \tilde{\chi}_1^0) = (550, 400)$ GeV events	47.2	20.7	123.7	97.0
$m(\tilde{t}_1, \tilde{\chi}_1^0) = (550, 430)$ GeV events	109.3	92.5	89.0	44.2
$m(\tilde{t}_1, \tilde{\chi}_1^0) = (550, 460)$ GeV events	106.4	70.8	36.0	20.4

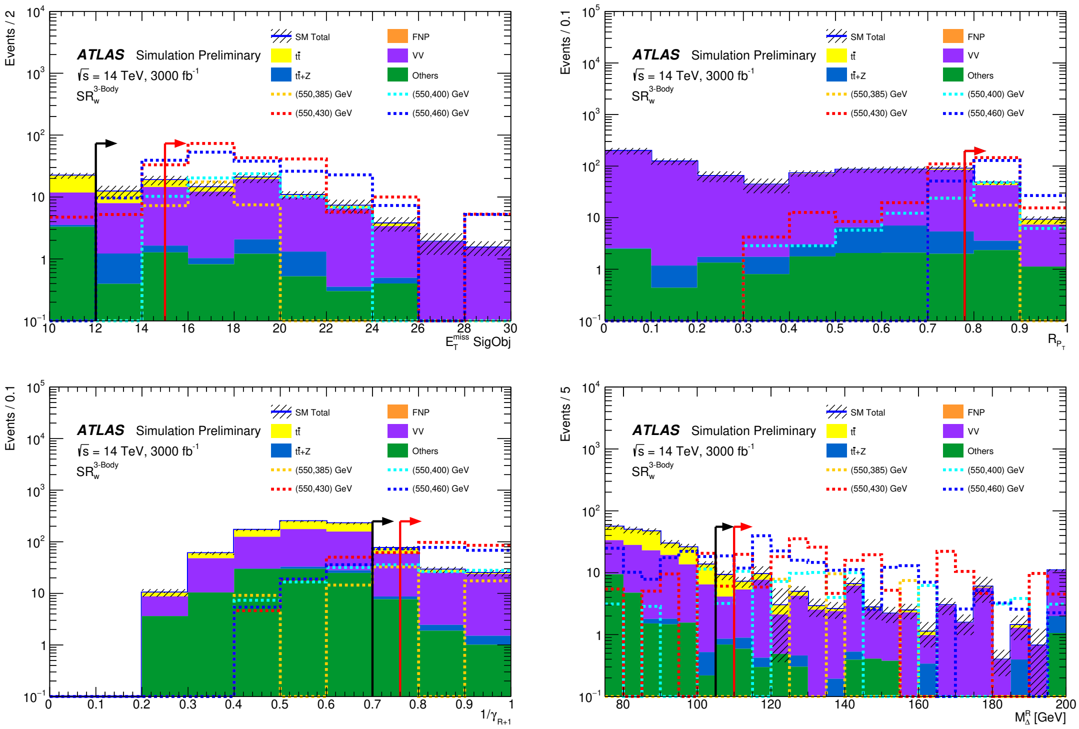

Figure 4: Distributions of the variables included in the optimised definition of $\mathrm{SR}_W^{3-\mathrm{body}}$ for the SM background and four signal benchmark points. All selection requirements are applied to the events entering these distributions but the cut on the plotted observable. Black and red arrows indicate the thresholds as used in Ref. [3] and in this note, respectively. The statistical uncertainty is shown on the total background as a shaded area. The final bin in each histogram includes the overflow.

plotted observable.

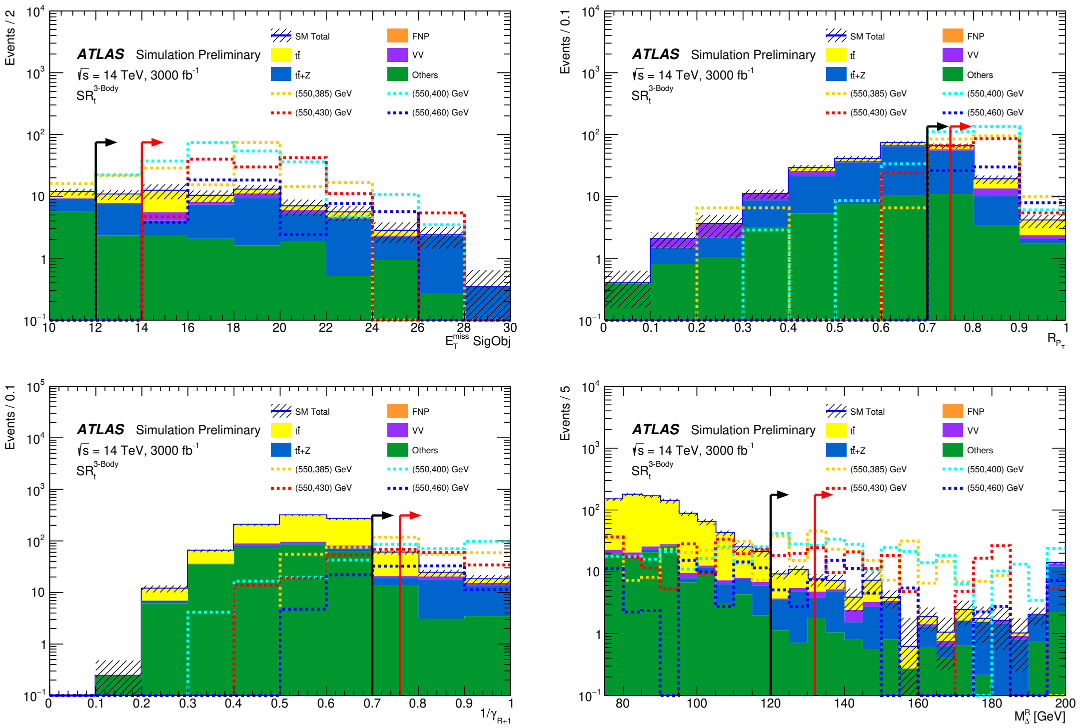

Figure 5: Distributions of the variables included in the optimised definition of $\mathrm{SR}_t^{3-\mathrm{body}}$ for the SM background and four signal benchmark points. All selection requirements are applied to the events entering these distributions but the cut on the plotted observable. Black and red arrows indicate the thresholds as used in Ref. [3] and in this note, respectively. The statistical uncertainty is shown on the total background as a shaded area. The final bin in each histogram includes the overflow.

6 Systematic uncertainties

Detector related systematic uncertainties are considered for all the SM background processes. They include uncertainties on electron and muon reconstruction efficiency, and on the energy or momentum scale and resolution [53, 54]. Uncertainties on the trigger efficiency are also considered [63–65]. The uncertainties on the jet energy scale and the jet energy resolution [66–68], and the jet flavour tagging uncertainties, related to the modelling of the b-tagging efficiencies for b-jets, c-jets and light-flavour jets are also considered [69, 70]. Energy and momentum scale uncertainties of electrons, muons and jets are propagated through the $E_{\mathrm{T}}^{\mathrm{miss}}$ calculation. Additional uncertainties on the $E_{\mathrm{T}}^{\mathrm{miss}}$ calculation account for the uncertainties on the "soft term" resolution and scale [61]. Systematic uncertainties on the theoretical description of the parton-level final states have been evaluated. They include uncertainties on the proton PDF, cross-section, and strong coupling constant. The uncertainties are estimated following the ATLAS physics modelling group prescriptions, essentially varying the renormalisation and factorisation scales, as well as the amount of initial- and final-state radiation. Additional uncertainties on the parton showering and hadronisation processes that convert partons into the hadronic final states are assessed comparing the two showering models implemented in Pythia and Herwig. These procedures are used for the main backgrounds like di-boson production, $t\bar{t}Z$ and $t\bar{t}$, for all other background processes which make minor contributions and for the signal samples a conservative estimate of the theoretical uncertainties is applied [3] (in the range 10% to 24% depending on $\Delta m(\tilde{t}_1, \tilde{\chi}_1^0)$).

Uncertainties are extrapolated to the HL-LHC conditions using a set of prescriptions commonly defined by CMS and ATLAS [71]. Theoretical uncertainties are expected to be reduced by half. Flavour tagging uncertainties are also expected to be reduced by half due to improvements in tracking and vertex performances. All other uncertainties like jet energy scale and resolution, $E_{\mathrm{T}}^{\mathrm{miss}}$ modelling and lepton modelling uncertainties including fake and non-prompt leptons estimate uncertainties, are expected to be similar to Ref. [3], where the systematic uncertainties in the data-driven FNP background estimate are expected due to potential differences in the FNP composition (heavy flavour, light flavour or photon conversions) between the analysis regions and the region used to extract the fake factor and the statistical error is also included by propagating the statistical uncertainty in the ratio used to compute the fake factor.

Table 6 summarises the contributions from the different sources of systematic uncertainty on the total SM background predictions for the three-body and four-body signal regions. ‘MC statistical uncertainty’ refers to the statistical uncertainty from the simulated event samples and it is one of the main contributions in all SRs, but it is expected to be significantly reduced by increasing the generation statistics. ‘Other theoretical uncertainties’ represents the theoretical uncertainty on the ‘Others’ background. ‘Normalisation’ takes into account the uncertainty on the data driven correction factors from the profile likelihood fit in Ref. [3]. The dominant uncertainty is related to the normalisation. Moving to the HL-LHC regime, such uncertainties will start to become more and more important as signal regions are not expected to remain statistically dominated. Future analyses will therefore benefit from dedicated studies, and current projections are considered conservative.

Table 6: Sources of systematic uncertainty in the SM background estimates. The values are given as relative uncertainties on the total expected background event yields in the SRs. Entries marked ‘–’ indicate a contribution smaller than 1%. The individual components can be correlated and therefore do not necessarily add up in quadrature to the total systematic uncertainty.

Signal Region	SR-DF$_{W}^{3-\mathrm{body}}$	SR-SF$_{W}^{3-\mathrm{body}}$	SR-DF$_{t}^{3-\mathrm{body}}$	SR-SF$_{t}^{3-\mathrm{body}}$	SR$^{4-\mathrm{body}}_{\mathrm{Small}\,\Delta m}$	SR$^{4-\mathrm{body}}_{\mathrm{Large}\,\Delta m}$
Total SM background uncertainty	14%	13%	13%	19%	14%	7.9%
VV theoretical uncertainties	10%	12%	1.4%	2.5%	8.9%	3.3%
$t\bar{t}$ theoretical uncertainties	2.8%	1.0%	3.7%	1.5%	1.5%	1.4%
$t\bar{t}$ +Z theoretical uncertainties	–	–	1.6%	2.4%	–	–
$t\bar{t}$–Wt interference	–	–	–	1.0%	1.0%	1.0%
Other theoretical uncertainties	–	–	1.2%	2.3%	–	–
MC statistical uncertainty	13%	9.5%	11%	15%	17%	5.3%
Normalisation	15%	17%	7.3%	8.9%	12%	10%
Jet energy scale	5.6%	7.5%	11%	20%	4.1%	4.8%
Jet energy resolution	8.9%	7.3%	11%	34%	3.5%	4.6%
Lepton modelling	3.0%	3.0%	5.3%	7.8%	6.9%	6.0%
$E_{\mathrm{T}}^{\mathrm{miss}}$ modelling	1.4%	1.0%	3.1%	5.7%	1.3%	1.0%
Flavour tagging	1.0%	1.0%	1.0%	1.7%	–	1.0%
Pile-up reweighting and JVT	2.6%	2.0%	1.0%	1.0%	3.1%	1.0%
Fake and non-prompt leptons	–	–	–	–	3.5%	6.7%

7 Results

The sensitivity is evaluated using the CLs method [72] in each signal region. A likelihood is built, using the HistFitter framework [73], as the product of Poissonian terms, one for each of the considered SRs. All systematic uncertainties, described earlier, are accounted for with Gaussian terms representing the assumed uncertainty. A profile likelihood ratio fit is performed for each signal point using pseudo-data corresponding to the sum of the expected background and the signal. Contours are shown indicating the regions in the stop-neutralino mass plane with 3σ and 5σ discovery potential, as well as the region that could be excluded, in case of no observation, at 95% confidence level using the HL-LHC full luminosity at 14 TeV. The signal regions in the two selections are combined for each signal point as described below.

7.1 Four-body expected sensitivities

The two signal regions of the four-body search are orthogonal and can be statistically combined. Figure 6 shows the four-body selection expected sensitivity contours with HL-LHC conditions in the $(m(\tilde{t}_1), m(\tilde{\chi}_1^0))$ and $(m(\tilde{t}_1), \Delta m(\tilde{t}_1, \tilde{\chi}_1^0))$ planes. The two signal regions are combined and the expected 3σ (green) and the 5σ (blue) discovery contours are shown as well as the expected 95% CL exclusion contour. This can be compared with the observed 95% CL exclusion contour from Ref. [3], also shown. The discovery sensitivity with a 5σ significance extends up to $m(\tilde{t}_1)$ of about 380 GeV for $\Delta m(\tilde{t}_1, \tilde{\chi}_1^0)$ of about 65 GeV and reaches about 480 GeV for $\Delta m(\tilde{t}_1, \tilde{\chi}_1^0)$ of about 25 GeV. The 95% CL exclusion limit extends up to $m(\tilde{t}_1)$ of about 690 GeV, for a $\tilde{\chi}_1^0$ mass of about 660 GeV.

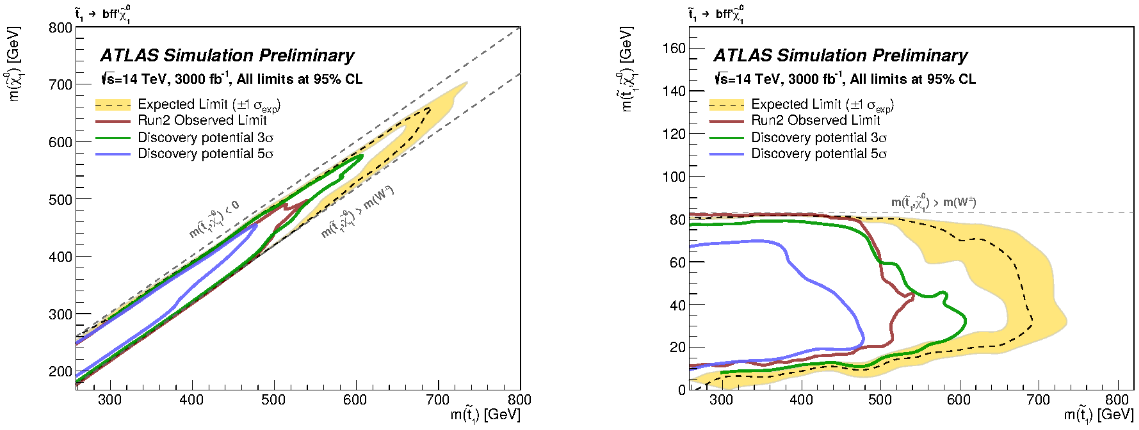

Figure 6: Four-body selection sensitivity contours in the plane $(m(\tilde{t}_1), m(\tilde{\chi}_1^0))$ (left plot) and in the plane $(m(\tilde{t}_1), \Delta m(\tilde{t}_1, \tilde{\chi}_1^0))$ (right plot) are shown. The expected 3σ (green) and the 5σ (blue) discovery contours and the expected 95% CL exclusion contour reachable at HL-LHC using the four-body selection for $\mathrm{SR}^{4-\mathrm{body}}_{\mathrm{Small}\,\Delta m}$ and $\mathrm{SR}^{4-\mathrm{body}}_{\mathrm{Large}\,\Delta m}$ are compared with the observed 95% CL exclusion contour using the Run 2 luminosity.

7.2 Three-body expected sensitivities

The three-body search signal regions are also orthogonal and they have been statistically combined. The expected sensitivity contours are shown in Figure 7. As in the previous section, the exclusion limits at

95% CL reachable with the HL-LHC luminosity are compared with the observed limits in Ref. [3] in the $(m(\tilde{t}_1), m(\tilde{\chi}_1^0))$ and $(m(\tilde{t}_1), \Delta m(\tilde{t}_1, \tilde{\chi}_1^0))$ planes and discovery sensitivity contours are shown. The discovery potential at 5σ extends up to stop masses of about 660 GeV for a $\tilde{\chi}_1^0$ mass of about 490 GeV in the three-body decay region and up to about 810 GeV for a massless $\tilde{\chi}_1^0$ in the two-body region. The exclusion sensitivity extends up to $m(\tilde{t}_1)$ of about 850 GeV for a $\tilde{\chi}_1^0$ mass of about 680 GeV in the three-body decay region and up to $m(\tilde{t}_1)$ of about 1010 GeV for a massless $\tilde{\chi}_1^0$ in the two-body decay region.

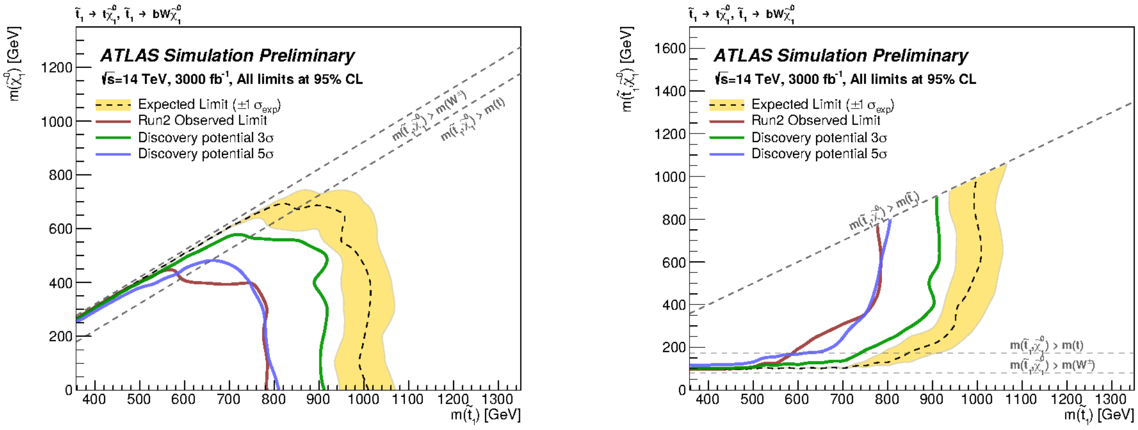

Figure 7: Three-body selection sensitivity contours in the plane $(m(\tilde{t}_1), m(\tilde{\chi}_1^0))$ (left) and in the plane $(m(\tilde{t}_1), \Delta m(\tilde{t}_1, \tilde{\chi}_1^0))$ are shown. The expected 3σ (green) and the 5σ (blue) discovery contours and the expected 95% CL exclusion contour reachable at HL-LHC using the three-body selection for $\mathrm{SR}_t^{3-\mathrm{body}}$ and $\mathrm{SR}_W^{3-\mathrm{body}}$ are compared with the observed 95% CL exclusion contour using full Run 2 luminosity.

7.3 Combined limits

The six signal regions described in Sec. 5 are mutually exclusive and can be statistically combined. Figure 8 shows the expected sensitivity contours for the statistical combination. The expected 3σ (green) and 5σ (blue) discovery contours and the expected 95% CL exclusion contour are shown in the plane $(m(\tilde{t}_1), m(\tilde{\chi}_1^0))$ (left plot) and in the plane $(m(\tilde{t}_1), \Delta m(\tilde{t}_1, \tilde{\chi}_1^0))$.

As result of the combination, the discovery potential at 5σ extends up to stop masses up to about 660 GeV for a $\tilde{\chi}_1^0$ mass of about 500 GeV in three-body decay region and up to about 820 GeV for a massless neutralino in the two-body region. The exclusion sensitivity extends up to $m(\tilde{t}_1)$ of about 730 GeV in the four-body region for a $\tilde{\chi}_1^0$ mass of about 670 GeV, up to $m(\tilde{t}_1)$ of about 860 GeV in the three-body decay region for a $\tilde{\chi}_1^0$ mass of about 690 GeV and up to $m(\tilde{t}_1)$ of about 1010 GeV in the two-body decay region for a massless neutralino.

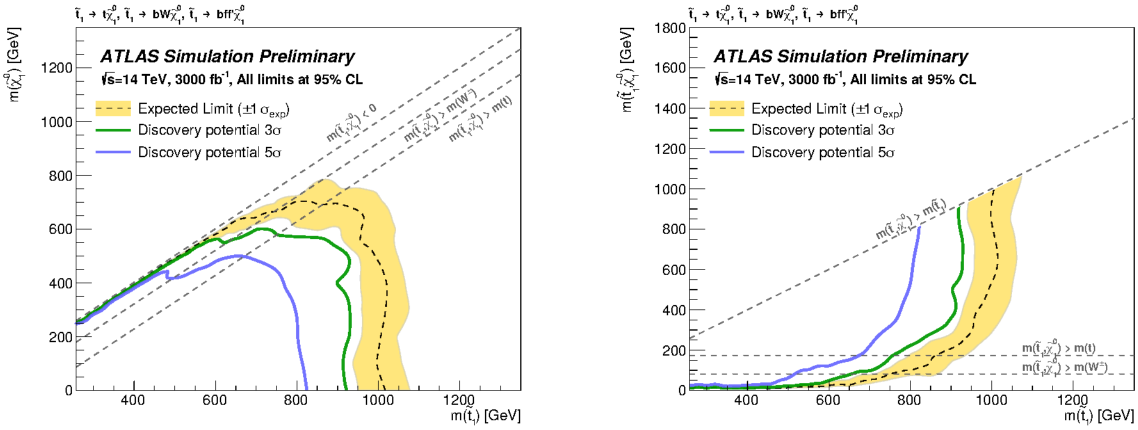

Figure 8: Sensitivity contours for the statistical combination of the four-body and three-body selections in the plane $(m(\tilde{t}_1), m(\tilde{\chi}_1^0))$ (left plot) and in the plane $(m(\tilde{t}_1), \Delta m(\tilde{t}_1, \tilde{\chi}_1^0))$ (right plot). The expected 3σ (green) and the 5σ (blue) discovery contours and the expected 95% CL exclusion contour reachable at HL-LHC are shown.

8 Conclusions

The sensitivity of the ATLAS experiment to stop pair production is investigated assuming 3000 fb^{-1} of proton-proton collisions at HL-LHC using an analysis strategy similar to the one published in a Run 2 search [3] in final states with two leptons, jets and missing transverse momentum. The estimate uses GEANT4 fully simulated background samples, generated at 13 TeV and scaled to the 14 TeV cross-sections. The stop samples are generated at 13 TeV, scaled for the cross-section changes with the centre of mass energy and processed through a simulation performed considering the layout and the response of the ATLAS detector, using the Run 2 layout and by applying a set of smearing functions at generator level to final-state particles. Experimental uncertainties for the background and the signal are based on the Run 2 results. The expected changes in systematic uncertainties due to upgraded detector, higher luminosity conditions and theoretical modelling are accounted by the use of scaling factors as defined by the ATLAS and CMS common working group for the HL-LHC. Two selections are optimised independently: a) in the four-body decay region, where $m(b) < \Delta m(\tilde{t}_1, \tilde{\chi}_1^0) < m(b) + m(W)$, and b) in the three-body decay region, where $m(W) + m(b) < \Delta m(\tilde{t}_1, \tilde{\chi}_1^0) < m(t)$; finally the second selection is also applied in the two-body decay region, where $\Delta m(\tilde{t}_1, \tilde{\chi}_1^0) > m(t)$.

Contours of expected 95% CL exclusion and 5σ discovery sensitivity in the plane of stop and neutralino masses are presented.

In the four-body decay region the discovery sensitivity with a 5σ significance extends up to $m(\tilde{t}_1)$ of about 380 GeV for $\Delta m(\tilde{t}_1, \tilde{\chi}_1^0)$ of about 65 GeV and reaches about 480 GeV for $\Delta m(\tilde{t}_1, \tilde{\chi}_1^0)$ of about 25 GeV. The discovery potential at 5σ extends up to stop masses of about 660 GeV for a $\tilde{\chi}_1^0$ mass of about 490 GeV in the three-body decay region and up to about 810 GeV for a massless $\tilde{\chi}_1^0$ in the two-body decay region. The 95% CL exclusion limit extends up to $m(\tilde{t}_1)$ of about 690 GeV, for a $\tilde{\chi}_1^0$ mass of about 660 GeV in the four-body decay region, up to $m(\tilde{t}_1)$ of about 850 GeV for a $\tilde{\chi}_1^0$ mass of about 680 GeV in the three-body decay region and up to $m(\tilde{t}_1)$ of about 1010 GeV for a massless $\tilde{\chi}_1^0$ in the two-body decay region, covering a significant region beyond the current limits.

As final remark, it is important to point out that the above results are expected to be conservative, since this analysis doesn't use the HL-LHC upgraded detector simulation, then it doesn't benefit from the extended coverage, or from the lower trigger thresholds. Moreover, significant potential improvements in object reconstruction and identification performance, in reduction of systematic uncertainties (both experimental and theoretical), and in analysis techniques can yield further enhancements beyond the anticipated gains from increased luminosity and cross-sections considered in the present studies.

References

[1] G. R. Farrar and P. Fayet, *Phenomenology of the production, decay, and detection of new hadronic states associated with supersymmetry*, Phys. Lett. B **76** (1978) 575.

[2] ATLAS Collaboration, *ATLAS sensitivity to top squark pair production at the HL-LHC*, ATL-PHYS-PUB-2018-021, 2028, URL: `https://cds.cern.ch/record/2644831/files/ATL-PHYS-PUB-2018-021.pdf`.

[3] ATLAS Collaboration, *Search for new phenomena in events with two opposite-charge leptons, jets and missing transverse momentum in pp collisions at* $\sqrt{s} = 13$ *TeV with the ATLAS detector*, JHEP **04** (2021) 165, arXiv: `2102.01444 [hep-ex]`.

[4] ATLAS Collaboration, *The ATLAS Experiment at the CERN Large Hadron Collider*, JINST **3** (2008) S08003.

[5] ATLAS Collaboration, *ATLAS Phase-II Upgrade Scoping Document*, CERN-LHCC-2015-020, LHCC-G-166, 2015, URL: `https://cds.cern.ch/record/2055248`.

[6] ATLAS Collaboration, *ATLAS Inner Tracker Strip Detector: Technical Design Report*, ATLAS-TDR-025; CERN-LHCC-2017-005, 2017, URL: `https://cds.cern.ch/record/2257755`.

[7] ATLAS Collaboration, *ATLAS Muon Spectrometer Phase-II Upgrade: Technical Design Report*, ATLAS-TDR-026; CERN-LHCC-2017-017, 2017, URL: `https://cds.cern.ch/record/2285580`.

[8] ATLAS Collaboration, *ATLAS LAr Calorimeter Phase-II Upgrade: Technical Design Report*, ATLAS-TDR-027; CERN-LHCC-2017-018, 2017, URL: `https://cds.cern.ch/record/2285582`.

[9] ATLAS Collaboration, *ATLAS Tile Calorimeter Phase-II Upgrade: Technical Design Report*, ATLAS-TDR-028; CERN-LHCC-2017-019, 2017, URL: `https://cds.cern.ch/record/2285583`.

[10] ATLAS Collaboration, *ATLAS TDAQ Phase-II Upgrade: Technical Design Report*, ATLAS-TDR-029; CERN-LHCC-2017-020, 2017, URL: `https://cds.cern.ch/record/2285584`.

[11] ATLAS Collaboration, *ATLAS Inner Tracker Pixel Detector: Technical Design Report*, ATLAS-TDR-030; CERN-LHCC-2017-021, 2017, URL: `https://cds.cern.ch/record/2285585`.

[12] ATLAS Collaboration, *A High-Granularity Timing Detector for the ATLAS Phase-II Upgrade: Technical Design Report*, ATLAS-TDR-031; CERN-LHCC-2020-007, 2020, URL: `https://cds.cern.ch/record/2719855`.

[13] ATLAS Collaboration, *Expected Tracking Performance of the ATLAS Inner Tracker at the HL-LHC*, ATL-PHYS-PUB-2019-014, 2019, URL: `https://cds.cern.ch/record/2669540`.

[14] GEANT4 Collaboration, S. Agostinelli et al., *GEANT4 – a simulation toolkit*, Nucl. Instrum. Meth. A **506** (2003) 250.

[15] ATLAS Collaboration, *Expected performance of the ATLAS detector at the High-Luminosity LHC*, ATL-PHYS-PUB-2019-005, 2019, URL: `https://cds.cern.ch/record/2655304/`.

[16] ATLAS Collaboration, *Formulae for Estimating Significance*, ATL-PHYS-PUB-2020-025, 2020, URL: https://cds.cern.ch/record/2736148.

[17] ATLAS Collaboration, *Measurement prospects of Higgs boson pair production in the $b\bar{b}\gamma\gamma$ final state with the ATLAS experiment at the HL-LHC*, ATL-PHYS-PUB-2022-001, 2022, URL: https://cds.cern.ch/record/2799146.

[18] ATLAS Collaboration, *Projected sensitivity of Higgs boson pair production combining the $b\bar{b}\gamma\gamma$ and $b\bar{b}\tau^+\tau^-$ final states with the ATLAS detector at the HL-LHC*, ATL-PHYS-PUB-2022-005, 2022, URL: https://cds.cern.ch/record/2802127.

[19] J. Alwall et al., *The automated computation of tree-level and next-to-leading order differential cross sections, and their matching to parton shower simulations*, JHEP **07** (2014) 079, arXiv: 1405.0301 [hep-ph].

[20] T. Sjöstrand et al., *An Introduction to PYTHIA 8.2*, Comput. Phys. Commun. **191** (2015) 159, arXiv: 1410.3012.

[21] P. Artoisenet, R. Frederix, O. Mattelaer, R. Rietkerk, *Automatic spin-entangled decays of heavy resonances in Monte Carlo simulations*, Journal of High Energy Physics **03** (2013) 015, arXiv: 1212.3460v2.

[22] R. D. Ball et al., *Parton distributions with LHC data*, Nucl. Phys. **B867** (2013) 244, arXiv: 1207.1303 [hep-ph].

[23] ATLAS Collaboration, *ATLAS Pythia8 tunes to 7 TeV data*, ATL-PHYS-PUB-2014-021, 2014, URL: http://cds.cern.ch/record/1966419.

[24] L. Lönnblad and S. Prestel, *Merging multi-leg NLO matrix elements with parton showers*, JHEP **03** (2013) 166, arXiv: 1211.7278 [hep-ph].

[25] ATLAS Collaboration, *Expected performance of the ATLAS detector under different High-Luminosity LHC conditions*, ATL-PHYS-PUB-2021-023, 2021, URL: https://cds.cern.ch/record/2776650.

[26] W. Beenakker, C. Borschensky, M. Krämer, A. Kulesza and E. Laenen, *NNLL-fast: predictions for coloured supersymmetric particle production at the LHC with threshold and Coulomb resummation*, JHEP **12** (2016) 133, arXiv: 1607.07741 [hep-ph].

[27] W. Beenakker et al., *NNLL resummation for squark and gluino production at the LHC*, JHEP **12** (2014) 023, arXiv: 1404.3134 [hep-ph].

[28] W. Beenakker et al., *Towards NNLL resummation: hard matching coefficients for squark and gluino hadroproduction*, JHEP **10** (2013) 120, arXiv: 1304.6354 [hep-ph].

[29] W. Beenakker et al., *NNLL resummation for squark-antisquark pair production at the LHC*, JHEP **01** (2012) 076, arXiv: 1110.2446 [hep-ph].

[30] W. Beenakker et al., *Soft-gluon resummation for squark and gluino hadroproduction*, JHEP **12** (2009) 041, arXiv: 0909.4418 [hep-ph].

[31] A. Kulesza and L. Motyka, *Soft gluon resummation for the production of gluino-gluino and squark-antisquark pairs at the LHC*, Phys. Rev. D **80** (2009) 095004, arXiv: 0905.4749 [hep-ph].

[32] A. Kulesza and L. Motyka,
Threshold Resummation for Squark-Antisquark and Gluino-Pair Production at the LHC,
Phys. Rev. Lett. **102** (2009) 111802, arXiv: `0807.2405 [hep-ph]`.

[33] W. Beenakker, R. Höpker, M. Spira and P. Zerwas,
Squark and gluino production at hadron colliders, Nucl. Phys. B **492** (1997) 51,
arXiv: `hep-ph/9610490`.

[34] T. Sjöstrand et al., *An introduction to PYTHIA 8.2*, Comput. Phys. Commun. **191** (2015) 159,
arXiv: `1410.3012 [hep-ph]`.

[35] P. Artoisenet, R. Frederix, O. Mattelaer and R. Rietkerk,
Automatic spin-entangled decays of heavy resonances in Monte Carlo simulations,
JHEP **03** (2013) 015, arXiv: `1212.3460 [hep-ph]`.

[36] S. Frixione, P. Nason and C. Oleari,
Matching NLO QCD computations with parton shower simulations: the POWHEG method,
JHEP **11** (2007) 070, arXiv: `0709.2092 [hep-ph]`.

[37] S. Alioli, P. Nason, C. Oleari and E. Re, *A general framework for implementing NLO calculations in shower Monte Carlo programs: the POWHEG BOX*, JHEP **06** (2010) 043,
arXiv: `1002.2581 [hep-ph]`.

[38] P. Nason, *A new method for combining NLO QCD with shower Monte Carlo algorithms*,
JHEP **11** (2004) 040, arXiv: `hep-ph/0409146`.

[39] M. Czakon and A. Mitov,
Top++: A program for the calculation of the top-pair cross-section at hadron colliders,
Comput. Phys. Commun. **185** (2014) 2930, arXiv: `1112.5675 [hep-ph]`.

[40] R. D. Ball et al., *Parton distributions for the LHC run II*, JHEP **04** (2015) 040,
arXiv: `1410.8849 [hep-ph]`.

[41] ATLAS Collaboration,
Modelling of the $t\bar{t}H$ *and* $t\bar{t}V$ $(V = W, Z)$ *processes for* $\sqrt{s} = 13$ *TeV ATLAS analyses*,
ATL-PHYS-PUB-2016-005, 2016, URL: `https://cds.cern.ch/record/2120826`.

[42] R. Frederix, E. Re and P. Torrielli,
Single-top t*-channel hadroproduction in the four-flavour scheme with POWHEG and aMC@NLO*,
JHEP **09** (2012) 130, arXiv: `1207.5391 [hep-ph]`.

[43] S. Alioli, P. Nason, C. Oleari and E. Re,
NLO single-top production matched with shower in POWHEG: s*- and* t*-channel contributions*,
JHEP **09** (2009) 111, arXiv: `0907.4076 [hep-ph]`, Erratum: JHEP **02** (2010) 011.

[44] M. Aliev et al., *HATHOR – HAdronic Top and Heavy quarks crOss section calculatoR*,
Comput. Phys. Commun. **182** (2011) 1034, arXiv: `1007.1327 [hep-ph]`.

[45] P. Kant et al., *HatHor for single top-quark production: Updated predictions and uncertainty estimates for single top-quark production in hadronic collisions*,
Comput. Phys. Commun. **191** (2015) 74, arXiv: `1406.4403 [hep-ph]`.

[46] N. Kidonakis,
Two-loop soft anomalous dimensions for single top quark associated production with a W^- *or* H^-,
Phys. Rev. D **82** (2010) 054018, arXiv: `1005.4451 [hep-ph]`.

[47] N. Kidonakis, 'Top Quark Production', *Proceedings, Helmholtz International Summer School on Physics of Heavy Quarks and Hadrons (HQ 2013)* (JINR, Dubna, Russia, 15th–28th July 2013) 139, arXiv: `1311.0283 [hep-ph]`.

[48] T. Gleisberg et al., *Event generation with SHERPA 1.1*, JHEP **02** (2009) 007, arXiv: `0811.4622 [hep-ph]`.

[49] ATLAS Collaboration, *Monte Carlo Generators for the Production of a W or Z/γ^* Boson in Association with Jets at ATLAS in Run 2*, ATL-PHYS-PUB-2016-003, 2016, URL: `https://cds.cern.ch/record/2120133`.

[50] R. Gavin, Y. Li, F. Petriello and S. Quackenbush, *FEWZ 2.0: A code for hadronic Z production at next-to-next-to-leading order*, (2010) 2388, arXiv: `1011.3540 [hep-ph]`.

[51] ATLAS Collaboration, *Multi-Boson Simulation for* 13 *TeV ATLAS Analyses*, ATL-PHYS-PUB-2017-005, 2017, URL: `https://cds.cern.ch/record/2261933`.

[52] H. B. Hartanto, B. Jäger, L. Reina and D. Wackeroth, *Higgs boson production in association with top quarks in the POWHEG BOX*, Phys. Rev. D **91** (2015) 094003, arXiv: `1501.04498 [hep-ph]`.

[53] ATLAS Collaboration, *Electron and photon performance measurements with the ATLAS detector using the 2015–2017 LHC proton–proton collision data*, JINST **14** (2019) P12006, arXiv: `1908.00005 [hep-ex]`.

[54] ATLAS Collaboration, *Muon reconstruction performance of the ATLAS detector in proton–proton collision data at $\sqrt{s} = 13$ TeV*, Eur. Phys. J. C **76** (2016) 292, arXiv: `1603.05598 [hep-ex]`.

[55] ATLAS Collaboration, *Measurement of the WW cross section in $\sqrt{s} = 7$ TeV pp collisions with ATLAS*, Phys. Rev. Lett. **107** (2011) 041802, arXiv: `1104.5225 [hep-ex]`.

[56] ATLAS Collaboration, *Search for anomalous production of prompt same-sign lepton pairs and pair-produced doubly charged Higgs bosons with $\sqrt{s} = 8$ TeV pp collisions using the ATLAS detector*, JHEP **03** (2015) 041, arXiv: `1412.0237 [hep-ex]`.

[57] CMS Collaboration, *Search for charged Higgs bosons with the $H^\pm \to \tau^\pm \nu_\tau$ decay channel in proton-proton collisions at* $\sqrt{s} = 13$ TeV, JHEP **07** (2019) 142, arXiv: `1903.04560 [hep-ex]`.

[58] CMS Collaboration, *Search for singly produced third-generation leptoquarks decaying to a τ lepton and a b quark in proton-proton collisions at* $\sqrt{s} = 13$ TeV, JHEP **07** (2018) 115, arXiv: `1806.03472 [hep-ex]`.

[59] ATLAS Collaboration, *Tagging and suppression of pileup jets with the ATLAS detector*, ATLAS-CONF-2014-018, 2014, URL: `https://cds.cern.ch/record/1700870`.

[60] ATLAS Collaboration, *ATLAS b-jet identification performance and efficiency measurement with $t\bar{t}$ events in pp collisions at $\sqrt{s} = 13$ TeV*, Eur. Phys. J. C **79** (2019) 970, arXiv: `1907.05120 [hep-ex]`.

[61] ATLAS Collaboration, *Performance of missing transverse momentum reconstruction with the ATLAS detector using proton–proton collisions at $\sqrt{s} = 13$ TeV*, Eur. Phys. J. C **78** (2018) 903, arXiv: `1802.08168 [hep-ex]`.

[62] ATLAS Collaboration,
Object-based missing transverse momentum significance in the ATLAS Detector,
ATLAS-CONF-2018-038, 2018, URL: `https://cds.cern.ch/record/2630948`.

[63] ATLAS Collaboration, *Performance of the ATLAS trigger system in 2015*,
Eur. Phys. J. C **77** (2017) 317, arXiv: `1611.09661 [hep-ex]`.

[64] ATLAS Collaboration, *Performance of electron and photon triggers in ATLAS during LHC Run 2*,
Eur. Phys. J. C **80** (2020) 47, arXiv: `1909.00761 [hep-ex]`.

[65] ATLAS Collaboration, *Performance of the ATLAS muon triggers in Run 2*,
JINST **15** (2020) P09015, arXiv: `2004.13447 [hep-ex]`.

[66] ATLAS Collaboration, *Jet energy scale measurements and their systematic uncertainties in proton–proton collisions at* $\sqrt{s} = 13$ *TeV with the ATLAS detector*, Phys. Rev. D **96** (2017) 072002,
arXiv: `1703.09665 [hep-ex]`.

[67] ATLAS Collaboration, *Jet energy scale and resolution measured in proton–proton collisions at* $\sqrt{s} = 13$ *TeV with the ATLAS detector*, Eur. Phys. J. C **81** (2020) 689,
arXiv: `2007.02645 [hep-ex]`.

[68] ATLAS Collaboration, *Determination of jet calibration and energy resolution in proton–proton collisions at* $\sqrt{s} = 8$ *TeV using the ATLAS detector*, Eur. Phys. J. C **80** (2020) 1104,
arXiv: `1910.04482 [hep-ex]`.

[69] ATLAS Collaboration, *Calibration of b-tagging using dileptonic top pair events in a combinatorial likelihood approach with the ATLAS experiment*, ATLAS-CONF-2014-004, 2014,
URL: `https://cds.cern.ch/record/1664335`.

[70] ATLAS Collaboration,
Calibration of the performance of b-tagging for c and light-flavour jets in the 2012 ATLAS data,
ATLAS-CONF-2014-046, 2014, URL: `https://cds.cern.ch/record/1741020`.

[71] *Addendum to the report on the physics at the HL-LHC, and perspectives for the HE-LHC: Collection of notes from ATLAS and CMS*, CERN Yellow Rep. Monogr. **7** (2019) Addendum,
arXiv: `1902.10229 [hep-ex]`.

[72] A. L. Read, *Presentation of search results: the* CL_S *technique*, J. Phys. G **28** (2002) 2693.

[73] M. Baak et al., *HistFitter software framework for statistical data analysis*,
Eur. Phys. J. C **75** (2015) 153, arXiv: `1410.1280 [hep-ex]`.

Appendix

Figure 9 shows the expected exclusion contour in the High Luminosity conditions obtained using the combination of the optimized $\mathrm{SR}^{4-\mathrm{body}}_{\mathrm{Small}\,\Delta m}$ and $\mathrm{SR}^{4-\mathrm{body}}_{\mathrm{Large}\,\Delta m}$, in comparison with the individual contribution of each SR to the exclusion contour.

Figure 10 shows the expected 95% CL exclusion contours using individually the four SRs in the three-body selection and the final combination.

Figure 11 shows the expected 95% CL exclusion contours using individually $\mathrm{SR}^{3-\mathrm{body}}_{t}$ and $\mathrm{SR}^{3-\mathrm{body}}_{W}$ (different flavour and same flavour are combined) and the final combination.

Figure 12 and Figure 13 show the expected 95% CL exclusion contours obtained in the statistical combination of the three-body and four-body SR selections. In Figure 12 the exclusion contours in the four body region and in the three body region are shown separately. In Figure 13 the $\Delta m(\tilde{t}_1, \tilde{\chi}^0_1)$ scale is logarithmic, in order to better highlight both small and large $\Delta m(\tilde{t}_1, \tilde{\chi}^0_1)$.

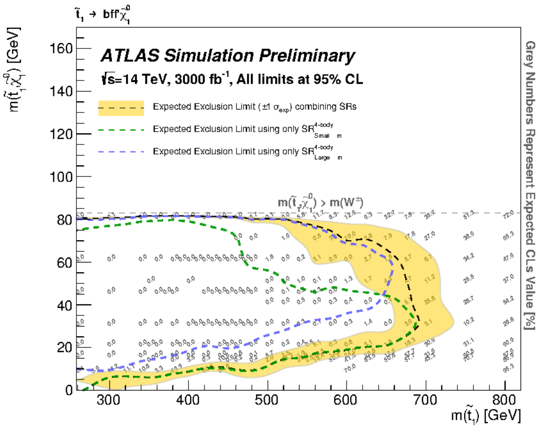

Figure 9: Expected exclusion limit in the High Luminosity conditions obtained using the combination of the optimized $\mathrm{SR}^{4-\mathrm{body}}_{\mathrm{Small}\,\Delta m}$ and $\mathrm{SR}^{4-\mathrm{body}}_{\mathrm{Large}\,\Delta m}$, compared with the exclusion limits obtained using each of the two SRs taken individually, in the $(m(\tilde{t}_1), \Delta m(\tilde{t}_1, \tilde{\chi}^0_1))$ plane.

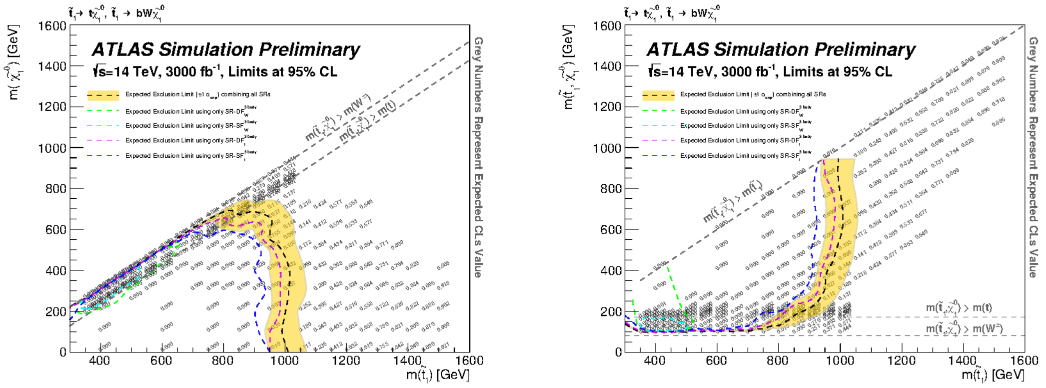

Figure 10: Three-body selection sensitivity contours: the expected 95% CL exclusion contour reachable at HL-LHC by using individually the 4 three-body SR selections, in the $(m(\tilde{t}_1), m(\tilde{\chi}_1^0))$ plane (left) and in the $(m(\tilde{t}_1), \Delta m(\tilde{t}_1, \tilde{\chi}_1^0))$ plane (right).

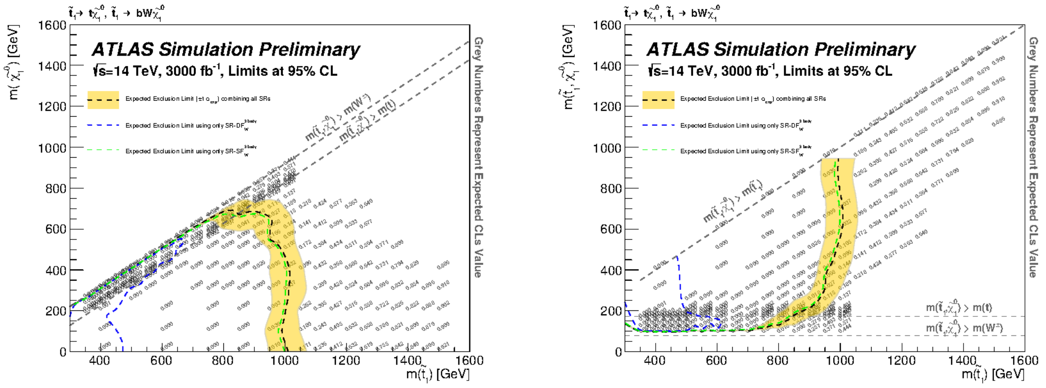

Figure 11: Three-body selection sensitivity contours: the expected 95% CL exclusion contour reachable at HL-LHC by using individually the three-body $\mathrm{SR}_t^{3-\mathrm{body}}$ and $\mathrm{SR}_W^{3-\mathrm{body}}$ (different flavour and same flavour are combined), in the $(m(\tilde{t}_1), m(\tilde{\chi}_1^0))$ plane (left) and in the $(m(\tilde{t}_1), \Delta m(\tilde{t}_1, \tilde{\chi}_1^0))$ plane (right).

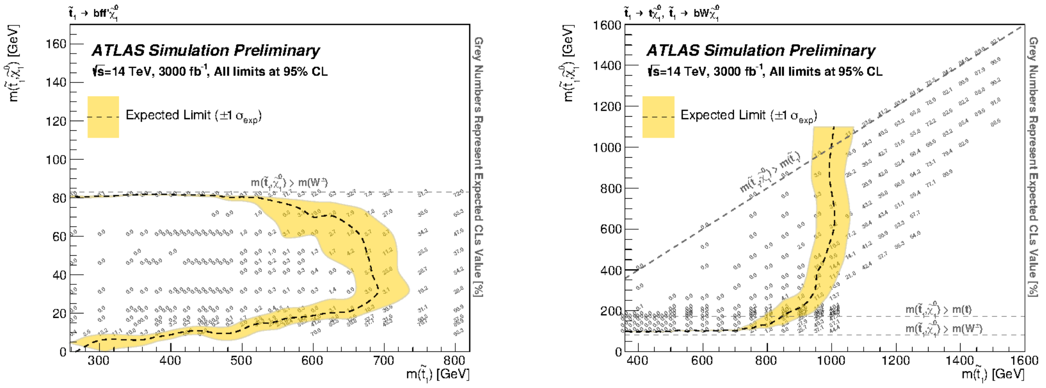

Figure 12: The 95% CL exclusion contour in the plane $(m(\tilde{t}_1), \Delta m(\tilde{t}_1, \tilde{\chi}_1^0))$ for the statistical combination of the three-body and four-body selections. Exclusion contours in the four body region (left) and in the three body region (right) are shown separately.

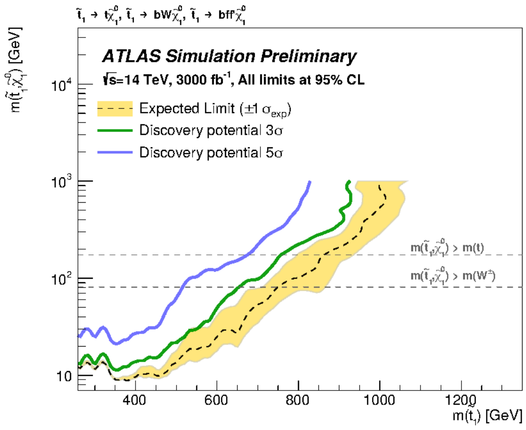

Figure 13: The 95% CL exclusion contour in the plane $(m(\tilde{t}_1), \Delta m(\tilde{t}_1, \tilde{\chi}_1^0))$ for the statistical combination of the three-body and four-body selections. $\Delta m(\tilde{t}_1, \tilde{\chi}_1^0)$ scale is logarithmic.